

The effect of aberration on partial-sky measurements of the cosmic microwave background temperature power spectrum

Donghui Jeong, Jens Chluba, Liang Dai, Marc Kamionkowski, and Xin Wang

Department of Physics and Astronomy, Johns Hopkins University, 3400 N. Charles St., Baltimore, MD 21218

(Dated: June 20, 2018)

Our motion relative to the cosmic-microwave-background (CMB) rest frame deflects light rays giving rise to shifts as large as $\ell \rightarrow \ell(1 \pm \beta)$, where $\beta = 0.00123$ is our velocity (in units of the speed of light) on measurements CMB fluctuations. Here we present a novel harmonic-space approach to this CMB aberration that improves upon prior work by allowing us to (i) go to higher orders in β , thus extending the validity of the analysis to measurements at $\ell \gtrsim \beta^{-1} \simeq 800$; and (ii) treat the effects of window functions and pixelization in a more accurate and computationally efficient manner. We calculate precisely the magnitude of the systematic bias in the power spectrum inferred from the partial sky, and show that aberration shifts the multipole moment by $\Delta\ell/\ell \simeq \beta \langle \cos\theta \rangle$, with $\langle \cos\theta \rangle$ averaged over the survey footprint. Such a shift, if ignored, would bias the measurement of the sound-horizon size θ_* at the 0.01%-level, which is comparable to the measurement uncertainties of Planck. The bias can then propagate into cosmological parameters such as the angular-diameter distance, Hubble parameter and dark-energy equation of state. We study the effect of aberration for current Planck, South Pole Telescope (SPT) and Atacama Cosmology Telescope (ACT) data and show that the bias cannot be neglected. We suggest that the small tension between Planck, ACT, and SPT may be due partially to aberration. An Appendix shows how the near constancy of the full-sky power spectrum under aberration follows from unitarity of the aberration kernel.

PACS numbers:

Keywords:

I. INTRODUCTION

Cosmic microwave background (CMB) radiation is very nearly isotropic in all directions with temperature of $\bar{T} = 2.7260 \pm 0.0013$ K [1]. There is, however, a temperature dipole ($\ell = 1$) in the CMB [2] that is now measured to have an amplitude $\Delta T \simeq 3.355 \pm 0.008$ mK along the direction $(l, b) = (263.99^\circ \pm 0.14^\circ, 48.26^\circ \pm 0.03^\circ)$ in Galactic coordinates [3]. Attributing the full dipole anisotropy to our motion with respect to the CMB rest frame suggests a speed of $v = 369 \pm 0.9$ km/s, or $\beta \equiv v/c = 0.00123$.

The CMB temperature also shows anisotropies, at the level of tens of μK , of primordial origin that are statistically isotropic in the rest frame of the CMB. However, our motion with respect to the CMB rest frame causes light aberration, a coherent modulation of the observed angular position of CMB photons from the original direction in the CMB rest frame. This leads to a dipolar departure from statistical isotropy: hot/cold spots observed in the direction of our motion appear to be smaller by a factor $\simeq (1 - \beta)$ than in the CMB rest frame, and *vice versa* in the opposite direction. The Planck collaboration recently detected this aberration [4] and confirmed that it is consistent with the velocity derived from the dipole anisotropy.

Most of the recent literature on light aberration traces back to Ref. [5] which considered the effects of aberration to $O(\beta^2)$ in full-sky CMB maps, concluding that aberration would lead to a correction $O(\beta^2) \simeq 10^{-6}$ to the values of cosmological parameters inferred by a full-sky CMB map. Refs. [6, 7] considered the detectability of the

off-diagonal correlations of temperature anisotropies induced by aberration, and Ref. [8] considered the effect of aberration on the angular scale of the acoustic peaks in the CMB power spectrum. Ref. [9] showed that the cancellations between the forward and backward directions in a full-sky map that lead to an $O(\beta^2)$ correction to the power spectrum do not arise in a partial-sky map. In this case, the effects of aberration on the inferred power spectrum appear at $O(\beta)$, and are thus considerably larger. Ref. [9] thus noted the significance of this effect for an experiment like Planck, which maps the full sky but masks out in the analysis portions of the sky obscured by foregrounds. The determination of cosmological parameters from these temperature anisotropies [10] may therefore be affected at $O(\beta)$.

It has also been noted that the analytic approach of Ref. [5], which works to $O(\beta^2)$, breaks down for multipole moments $\ell \gtrsim \beta^{-1} \simeq 800$ [e.g., see 5, 18]. Thus, for experiments like Planck [11], the South Pole Telescope (SPT) [12, 13], and the Atacama Cosmology Telescope (ACT) [14, 15], which make high-angular-resolution precision measurements of CMB fluctuations, something more must be done. Refs. [16, 17] thus proposed to deal with this issue by “de-boosting” the CMB map in real-space; i.e., using the magnitude and direction of the temperature dipole to Lorentz transform the observed CMB temperature to the rest frame. As we show below, however, this real-space de-boosting does not easily account for effects associated with pixelization and a finite window function, issues that arise from the Lorentz transformation of the solid angle from the observer frame to the rest frame.

Here we employ a harmonic-space approach to CMB

aberration. We adopt the recursive calculation of Ref. [18] to include the effects of aberration to higher orders in β and thus to treat maps with very high resolution. It also provides, as we show below (and argued in Ref. [18]), a far more effective and computationally efficient way to include the effects of pixelization and window function. To be a bit more precise, we combine the real- and harmonic-space approaches. We first generate Gaussian random realizations for a given power spectrum in harmonic space and then include the effects of aberration by transforming the $a_{\ell m s}$ with the harmonic-space aberration kernel from Ref. [18]. We then transform these harmonic coefficients to real space to apply the masks by multiplying the masking function (1 for the observed pixel, 0 otherwise). Finally, we measure the angular power spectrum from the masked real-space map. We repeat this procedure many times to study systematic changes in the resulting angular power spectrum and compare the resulting angular power spectrum to the masked angular power spectrum without aberration. As we show below, this approach accounts for mask window-function effects more accurately with less computational effort.

We then apply these calculations to determine the effects of aberration on SPT and ACT (and also Planck). As we will see, the magnitude of the aberration correction to the ACT/SPT power spectra are closer to $\simeq 1\%$, rather than $O(\beta) \simeq 0.1\%$. This is because the power spectrum scales roughly as $C_\ell \propto \ell^{-7}$ for $1000 \lesssim \ell \lesssim 3000$ and because aberration leads (in the forward/backward direction) to a re-scaling $\ell \rightarrow \ell(1 \pm \beta)$. The fractional change to the power spectrum is thus $(\Delta C_\ell / C_\ell) \simeq 7\beta \simeq 0.01$, and even larger in regimes where the acoustic oscillations increase $\partial C_\ell / \partial \ell$. This correction is thus comparable in magnitude to the statistical error in these experiments and is thus a systematic correction that *must* be taken into account in measurement. It is thus imperative to perform the correction carefully, as we do below.

This paper is organized as follows. We begin in Sec. II by reviewing the effect of aberration on the full sky. Then, in Sec. III, we discuss simulations of aberration on the full sky including the effects of pixelization and the window function. Sec. IV then discusses measurements of the power spectrum on the cut sky. After considering some illustrative examples, we calculate explicitly the effects of aberration on the power spectra inferred in Planck, ACT (both the equatorial and southern surveys), and SPT. We conclude in Sec. V. An Appendix discusses the unitarity of the aberration kernel and shows why the effects of aberration on the full-sky power spectrum remain small even at $\ell \gtrsim 800$.

II. ABERRATION ON THE FULL SKY

A. Basics: CMB aberration

Let us denote the 4-momentum of a CMB photon by $p^\mu = (E, \mathbf{p})$ in the CMB rest frame and $p'^\mu = (E', \mathbf{p}')$ in the observer's frame. For simplicity, let us align the z axis with the direction of the observer's motion with respect to the CMB rest frame. Then, the two 4-momenta are related by a Lorentz boost,

$$\begin{pmatrix} E \\ p_x \\ p_y \\ p_z \end{pmatrix} = \begin{pmatrix} \gamma & 0 & 0 & \gamma\beta \\ 0 & 1 & 0 & 0 \\ 0 & 0 & 1 & 0 \\ \gamma\beta & 0 & 0 & \gamma \end{pmatrix} \begin{pmatrix} E' \\ p'_x \\ p'_y \\ p'_z \end{pmatrix}. \quad (1)$$

Here, $\beta = v/c$, and $\gamma = 1/\sqrt{1-\beta^2}$. Consider a CMB photon seen in the CMB rest frame in the direction $-\hat{\mathbf{p}} = \hat{\mathbf{n}} = (\sin\theta, 0, \cos\theta)$. Then, we observe the photon from the direction $-\hat{\mathbf{p}}' = \hat{\mathbf{n}}' = (\sin\theta', 0, \cos\theta')$ where

$$\cos\theta' = \frac{\cos\theta + \beta}{1 + \beta\cos\theta}. \quad (2)$$

Under this transformation, the solid-angle element transforms as

$$d\Omega' = \frac{d\Omega}{\gamma^2(1 + \beta\cos\theta)^2}, \quad (3)$$

which means that the observed solid angle covered by a bundle of CMB photons is different than that in the CMB rest frame. As a result, the angular separation $\Delta\theta$ in the CMB rest frame is observed to be

$$\Delta\theta' = \frac{\Delta\theta}{\gamma(1 + \beta\cos\theta)} \simeq \Delta\theta [1 - \beta\cos\theta + \mathcal{O}(\beta^2)]. \quad (4)$$

That is, when considering typical cold or hot spots of $\simeq 1$ deg, those spots shrink toward the direction of our motion ($\theta = 0$) and expand toward the opposite direction ($\theta = \pi$). Therefore, the temperature (and polarization) anisotropies show a dipolar distortion in their shape, which we call *aberration*.

The specific intensities in the CMB rest frame and observer frame are related by

$$I_{\nu'}(\hat{n}') = \frac{\nu'^3}{\nu^3} I_\nu(\hat{n}), \quad (5)$$

with $\nu = \gamma(1 - \beta\cos\theta')\nu'$ and \hat{n}' and \hat{n} being related by Eq. (2). If the specific intensity in the CMB rest frame is a Planck function with temperature $T(\hat{n}) = \bar{T}[1 + \Delta_T(\hat{n})]$,

$$I_\nu(\hat{n}) = \frac{2h\nu^3}{c^2} \left[\exp\left(\frac{h\nu}{k_B T(\hat{n})}\right) - 1 \right]^{-1}, \quad (6)$$

then the intensity in the observed frame is given by

$$I_{\nu'}(\hat{n}') = \frac{2h\nu'^3}{c^2} \left[\exp\left(\frac{h\nu'\gamma(1 - \beta\mu')}{k_B T(\hat{n})}\right) - 1 \right]^{-1}, \quad (7)$$

which is, again, a Planck function with observed temperature

$$T_{\text{obs}}(\hat{n}') = \frac{T(\hat{n})}{\gamma(1 - \beta\mu')}. \quad (8)$$

This is the key equation of aberration which relates the observed temperature at direction \hat{n}' to the intrinsic CMB temperature $T(\hat{n})$.

B. Aberration in harmonic space

In spherical-harmonic space, the aberration in Eq. (8) is written as a linear transformation¹ [5],

$$a_{\ell m}^{(\text{obs})}(\beta) = \sum_{\ell' m'} \mathcal{K}_{\ell m}^{\ell' m'}(\beta) a_{\ell' m'}, \quad (9)$$

of the spherical-harmonic coefficients. Here $\mathcal{K}_{\ell m}^{\ell' m'}$ is the aberration kernel which depends on the amplitude β and direction $\hat{\beta}$ of the observer's velocity in the CMB rest frame. We indicate the observed spherical-harmonic coefficients in the moving observer's frame by a subscript (obs). The kernel, obtained from Eq. (8), is

$$\mathcal{K}_{\ell m}^{\ell' m'}(\beta) = \int \frac{d^2\Omega'}{\gamma(1 - \beta \cdot \hat{\mathbf{n}}')} Y_{\ell' m'}(\hat{n}) Y_{\ell m}^*(\hat{n}'). \quad (10)$$

When we choose the coordinate system so that the observer's moving direction is aligned to the pole ($\theta = 0$), the azimuthal symmetry allows the kernel to be simplified to

$$\mathcal{K}_{\ell m}^{\ell' m'}(\beta \hat{\mathbf{z}}) \equiv \mathcal{K}_{\ell m}^{\ell' m}(\beta) \delta_{mm'}, \quad (11)$$

where

$$\mathcal{K}_{\ell m}^{\ell' m}(\beta) = 2\pi \mathcal{N}_{\ell m} \mathcal{N}_{\ell' m} \int_{-1}^1 \frac{P_{\ell'}^m(\mu) P_{\ell}^m(\mu')}{\gamma(1 - \beta\mu')} d\mu', \quad (12)$$

in terms of associate Legendre polynomials $P_{\ell}^m(\mu)$ and the normalization factor

$$\mathcal{N}_{\ell m} = \sqrt{\frac{(2\ell + 1)(\ell - m)!}{4\pi(\ell + m)!}}, \quad (13)$$

of the spherical harmonics. We evaluate the aberration kernel $\mathcal{K}_{\ell m}^{\ell' m}$ to higher orders in β by using a recursion relation described in [18]. Note that the kernel satisfies the relations,

$$\mathcal{K}_{\ell m}^{\ell' m}(\beta) = (-1)^{\ell + \ell'} \mathcal{K}_{\ell' m}^{\ell m}(\beta), \quad (14)$$

$$\mathcal{K}_{\ell - m}^{\ell' - m}(\beta) = \mathcal{K}_{\ell m}^{\ell' m}(\beta), \quad (15)$$

so it suffices to calculate only a quarter of all the matrix elements.

The kernel $\mathcal{K}_{\ell m}^{\ell' m}$ quantifies how much power is transferred from intrinsic CMB multipole coefficients $a_{\ell' m}$ to $a_{\ell m}^{(\text{obs})}$. Eq. (12) therefore says that (1) aberration does not alter the component of angular momentum in the direction $\hat{\beta}$ of the moving observer; and (2) power transfer from $a_{\ell m}$ to $a_{\ell + \Delta\ell, m}^{(\text{obs})}$ is most efficient for $\Delta\ell \lesssim \beta\ell$ and sharply decays for larger $\Delta\ell$. For details of the aberration kernel, including the $\Delta\ell$ and m dependence, we refer the reader to Ref. [18].

C. Aberrated CMB two-point functions

Statistical isotropy dictates that the spherical-harmonic coefficients $a_{\ell m}$ of the CMB map, in its rest frame, are statistically independent. However, aberration induces correlations between different observed spherical-harmonic coefficients $a_{\ell m}^{(\text{obs})}$.

Here, and throughout, we define m with respect to the moving direction, so that Eq. (11) holds. Then, the two-point correlator of temperature anisotropies becomes

$$\begin{aligned} & \left\langle a_{\ell_1 m_1}^{(\text{obs})} a_{\ell_2 m_2}^{(\text{obs}) *} \right\rangle \\ &= \sum_{\ell'_1 \ell'_2 m'_1 m'_2} \mathcal{K}_{\ell_1 m_1}^{\ell'_1 m'_1}(\beta) \mathcal{K}_{\ell_2 m_2}^{\ell'_2 m'_2}(\beta) \left\langle a_{\ell'_1 m'_1} a_{\ell'_2 m'_2}^* \right\rangle \\ &= \sum_{\ell'_1 \ell'_2 m'_1 m'_2} \mathcal{K}_{\ell_1 m_1}^{\ell'_1 m_1}(\beta) \delta_{m_1 m'_1} \mathcal{K}_{\ell_2 m_2}^{\ell'_2 m_2}(\beta) \delta_{m_2 m'_2} C_{\ell'_1} \delta_{\ell'_1 \ell'_2} \delta_{m'_1 m'_2} \\ &= \sum_{\ell'} \mathcal{K}_{\ell_1 m_1}^{\ell' m_1}(\beta) \mathcal{K}_{\ell_2 m_2}^{\ell' m_2}(\beta) C_{\ell'} \delta_{m_1 m_2}. \end{aligned} \quad (16)$$

III. SIMULATING THE EFFECTS OF ABERRATION

In order to simulate the combined effect of aberration and sky masking (the subject of the following Section) we must first generate the temperature map in the observed frame. A Gaussian realization of the temperature map in the CMB rest frame is easily obtained from a given angular power spectrum. Once a map of the temperature in the CMB rest frame is given, the effects of aberration can be added in both real and harmonic space.

In real space, we add aberration by applying Eq. (8) to the simulated Gaussian temperature map. As the simulated map is given in discretized pixels, we aberrate it in a pixel-by-pixel manner. We find it more convenient to apply Eq. (8) backward rather than forward. Namely, for a pixel at location \hat{n}' in the observed frame, we find $\Delta_T(\hat{n})$, with \hat{n} given by Eq. (2), from the temperature in the CMB rest frame. Then, applying the μ' -dependent modulation provides the effect of aberration. If we had alternatively started with pixels in the CMB rest frame, we would have additionally needed to take into account

¹ There is a correction that arises from the fact that the mean temperature of the boosted map is different than that of the original map [18]. However, except for the temperature dipole which is linear in β , this correction is tiny, $O(\beta^2)$, and so we neglect it below.

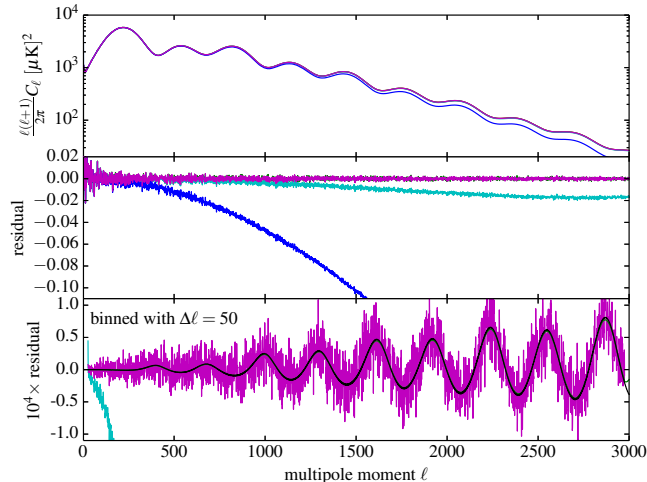


FIG. 1: Angular power spectra and their residual $\Delta C_\ell/C_\ell$ for simulated full-sky temperature maps. The angular power spectra are averaged over 500 Gaussian realizations after taking the effect of our motion into account using real-space boosting (blue) or harmonic-space boosting (magenta). The central panel shows the residual relative to the input theoretical power spectrum, and the bottom panel shows the residual with respect to the power spectrum estimated from the un-aberrated Gaussian temperature map. Thus, the cosmic variance cancels out in the bottom panel. Further, to reduce the scatter to the 10^{-5} level, we take a moving average with width $\Delta\ell = 50$ in the bottom panel. The black solid curve in the bottom panel shows the residual predicted from the aberration kernel and input theoretical power spectrum, and the green solid curve, which lies behind the black curve, in the bottom panel shows the analytical approximation in Eq. (24) with $\langle \cos^2 \theta \rangle = 1/3$. While harmonic-space boosting yields the aberrated angular power spectrum consistent with the theory prediction, real-space boosting shows strong power suppression for $\ell \gtrsim 300$. Deconvolution of the window function (cyan) restores somewhat the power on larger angular scales ($\ell \lesssim 500$), to within a percent level, but the deviation remains as large as $\simeq 2\%$ at $\ell \simeq 2500$ because of aliasing and imperfect knowledge of the exact pixel window function in HEALPIX.

the changes [Eq. (3)] in the solid angle of each pixel. This simple procedure was used in Ref. [18] to illustrate the effect of our motion on the CMB sky.

The harmonic-space approach makes use of the aberration kernel $\mathcal{K}_{\ell m}^{\ell' m}(\beta)$ calculated in Sec. II B. To ensure the convergence of the harmonic-space kernel, we choose rather stringent parameters in the kernel calculation: mode mixing to $|\ell' - \ell| = 10$ and terms to β^{40} , or $\Delta\ell = 10$ and $k_{\max} = 20$ in terms of parameters in Ref. [18]. With these settings the effect of aberration can be modeled quasi-exactly up to $\ell \simeq 4000$. Once the kernel is calculated for a given observer velocity β , we calculate the $a_{\ell' m}^{(\text{obs})}$ from the simulated Gaussian map $a_{\ell m}$ in harmonic space.

We generated 500 Gaussian temperature maps using

the WMAP7 best-fit power spectrum [19] using HEALPIX [20]² with $N_{\text{side}} = 2048$ ($L_{\max} = 4000$). We then simulate aberration by using both real-space and harmonic-space boosting. The resulting power spectra averaged over the realizations and their residuals are shown in Fig. 1. The upper panel shows the averaged angular power spectrum. On the full sky, an accurate simulation of the effect of aberration must yield a temperature power spectrum close to the non-aberrated one [5]. While the angular power spectrum from the aberrated map using the harmonic-space kernel (magenta curve) is consistent with the input power spectrum, the angular power spectrum obtained with real-space boosting (blue curve) shows a significant power suppression on smaller angular scales. We facilitate the comparison better by dividing the aberrated angular power spectrum by the input power spectrum in the central panel. For $N_{\text{side}} = 2048$, real-space boosting causes a suppression of the power spectrum by 5% at $\ell \simeq 1000$ and the suppression becomes larger on smaller scales (larger ℓ).

This suppression of power in real-space boosting was also found in Refs. [16, 17]. There, to correct for aberration, the authors inverted Eq. (8) in real space to recover the intrinsic temperature map from the observed $\Delta'_T(\hat{n}')$. In their numerical study of real-space deboosting, Ref. [17] report the suppression in the recovered angular power spectrum relative to the input power spectrum, and find that a HEALPIX resolution of $N_{\text{side}} = 8192$ or greater is required to achieve 1% accuracy in the recovered angular power spectrum to $\ell = 2000$. Performing this analysis with such a high resolution is computationally intensive and impractical with current computational power. Harmonic-space boosting thus provides significant computational advantages.

1. Effect of the pixel window function

The power suppression in real-space boosting occurs when applying the coordinate transformation from the moving frame to the CMB rest frame: the pixel center in the observed frame is not necessarily mapped into the pixel center in the CMB rest frame, and *vice versa*. Therefore, aberration of a given temperature map in the CMB rest frame always involves interpolation to calculate the temperature anisotropy at the mapped off-center point.

A generic interpolation scheme is formulated as the convolution between pixelized temperature anisotropies and the interpolating window function W :

$$\Delta_T(\hat{n}) = \sum_i W(\hat{n} - \hat{n}_i) \Delta_T^{(\text{pixel})}(\hat{n}_i). \quad (17)$$

² <http://healpix.jpl.nasa.gov>

Here, \hat{n}_i is the angular position of i -th pixel-center. The interpolating window function W depends on the interpolation scheme, but, in general, the shape and size of the discretized pixel are most important. For example, for the nearest-grid-point (NGP) interpolation, where $\Delta_T(\hat{n})$ takes the value at the nearest pixel point, W is the pixel shape itself [$1/(\text{Area of pixel})$ for the points inside of pixel, and 0 otherwise], and for the cloud-in-cell (CIC) interpolation, where $\Delta_T(\hat{n})$ is given by the weighted—weighting factor is proportional to the proximity—sum of the four nearby $\Delta_T(\hat{n}_i)$'s, the window function W is given by the convolution of two pixel shapes. In harmonic space, convolution in Eq. (17) implies that the resulting harmonic coefficients are given by the multiplication of temperature anisotropies and the interpolating window function $w_{\ell m}$:

$$a_{\ell m}^{(\text{pixel})} = w_{\ell m}^{(\text{pixel})} a_{\ell m}. \quad (18)$$

Since it is localized in real space, the interpolating window function is unity for $\ell \lesssim \pi/(\Delta\theta)$ but decreases for small scales $\ell \gtrsim \pi/(\Delta\theta)$ where $\Delta\theta$ is the angular resolution. Therefore, the angular power spectrum of the aberrated map generated with real-space boosting is expected to show power suppression on smaller scales according to the shape of the window function W of the interpolation.

Now that we know that power suppression is due to the interpolation window function, we may remedy the situation by de-convolving the window function in harmonic space. As we used the cloud-in-cell scheme, the interpolating window function is given by

$$W_\ell \equiv [w_\ell(\text{pixel})]^2, \quad (19)$$

where $w_\ell \simeq \text{sinc}(\ell\Delta\theta/2\pi)$ is the pixel window function of HEALPIX. Then, we deconvolve the aberrated power spectrum as

$$C_\ell^{(\text{deconvolve})} = W_\ell^{-2} C_\ell^{(\text{aberration})}. \quad (20)$$

The cyan curves in Fig. 1 show the result of deconvolution by dividing the angular power spectrum from real-space boosting by the harmonic transform of the HEALPIX window function. The de-convolved angular power spectrum is somewhat improved relative to the severe power suppression at multipoles $\ell \lesssim 500$, but it still deviates at $\lesssim 2\%$ on smaller scales ($\ell \gtrsim 2000$) from the input power spectrum. We attribute these residuals to the imperfect knowledge of the HEALPIX window function. In fact, because each pixel in HEALPIX is not identical, it is almost impossible to perfectly calculate the pixel window function. In addition, aliasing due to the finite pixelization may also hamper the deconvolution.

To summarize, since the coordinate transformation Eq. (2) is defined in real space, simulating the effect of aberration may be easier in real space than in harmonic space, where one has to separately calculate the kernels. In practice, however, we find the harmonic-space

approach superior because the finite resolution and associated pixel window function plagues the real-space simulations. Therefore, in the following Section, we simulate aberration in harmonic space.

2. The effect of aberration effect on the full-sky angular power spectrum

Although only up to 0.01%, the aberrated angular power spectrum do show systematic residual $\Delta C_\ell/C_\ell$ compared to the un-aberrated one. The bottom panel of Fig. 1 shows detailed shape of the power spectrum residual. To capture such a small residual from 500 simulations, we first divide aberrated power spectrum by the power spectrum estimated from the un-aberrated Gaussian temperature map so that the cosmic variance cancels out. Then, we further reduce the scatter by taking a moving average with width $\Delta\ell = 50$ for harmonic-space boosting (magenta curve) and real-space boosting (cyan curve). For comparison, the black solid curve shows the theoretical prediction calculated from the input power spectrum and aberration kernel with Eq. (16). Again, the power spectrum from harmonic-space boosting lies right on top of the theory prediction, while real-space boosting, even after the deconvolution, fails to catch up with the correct result.

We observe that the residual due to aberration increases toward the smaller angular scales and oscillates roughly, but not exactly, in-phase with the second derivative of the angular power spectrum: $d^2 C_\ell/d\ell^2$. This can be understood from unitarity as well as the symmetric shape of the aberration kernel. We discuss in App. A and in the discussion around Eq. (24) in the next Section the analytical approximation of the residual which is shown as a green line in the bottom panel of Fig. 1. Note that the analytical approximation (green curve) is so accurate that it is hard to distinguish from the exact theory calculation (black curve).

IV. ABERRATION ON A CUT SKY

In the previous Section, we studied the effects of aberration on full-sky CMB temperature maps. In reality, however, we never perform analyses on the full sky. Planck masks out regions with bright foregrounds, and more importantly, suborbital experiments like SPT and ACT are restricted to a small patch of sky. In particular, high-resolution surveys like SPT and ACT measure the CMB power spectrum at $\ell \gg \beta^{-1}$ where aberration might be important. In this Section, we demonstrate that aberration introduces a systematic bias on the small-scale CMB power spectrum if the sky mask is significantly asymmetric with respect to the equatorial plane of aberration.

Using the harmonic-space boosting approach, outlined in Sec. III, we simulate both aberrated and unaberrated

maps of the CMB assuming $\beta = 10^{-3}$ and measure the angular power spectrum only from the masked regions in real space to examine the fractional change in the cut-sky power spectrum induced by aberration³. As we will see, the effect of aberration on the cut-sky power spectrum depends sensitively on the *shape* and *location* of the masked region. When the masked region is symmetrically distributed in the forward/backward direction with respect to our peculiar velocity, the effect of aberration is essentially the same as in the full-sky case. On the other hand, when the masked region contains more in the forward (backward) direction, the aberrated power spectrum is enhanced (suppressed) compared to the unaberrated power spectrum. Therefore, ACT and SPT, both of which are aimed largely in the backward direction, suffer from power suppression as large as 1%, and the high-frequency channel of Planck is also affected by aberration at the level comparable to the cosmic-variance error on smaller scales. A bias at this level can result in discrepancies between these CMB experiments if aberration is not accounted for, as we demonstrate below.

A. Illustrative examples

To illustrate the effect of aberration on the cut-sky power spectrum, we first consider a few toy masks with regular shapes in Fig. 2. In the top panel, the Mollweide-projected sky map is presented in a coordinate system where the direction of the observer’s peculiar velocity aligns with the north pole. Each of the five “ring”-shaped cut skies considered here occupies a narrow range of latitudes in the forward hemisphere (northern hemisphere) with the same sky coverage $f_{\text{sky}} = 0.1$. However, each is located at a different range of latitudes. We call them `ring0` to `ring4` from top (higher latitude) to bottom (lower latitude). The five plots in the bottom panel show the fractional difference $\Delta C_\ell/C_\ell$ of the aberrated power spectra (with $\Delta\ell = 50$ binning) from the unaberrated power spectra, for each of the five cut skies, respectively. Cyan dots show the fractional differences between power spectra directly measured from the cut skies while blue dots (which lies on top of the cyan dots for small ℓ) show the difference after deconvolving the cut-sky masking effect by inverting the coupling matrix in the MASTER algorithm [21].⁴ The black dashed curve following the cyan dots shows the moving average of the residuals with

$\Delta\ell = 50$. In the bottom plots, for reference, we also show the cosmic variance for $f_{\text{sky}} = 0.1$ as red dashed curves, and indicate the un-biased case ($\Delta C_\ell/C_\ell = 0$) with black solid curves.

The residual plots in Fig. 2 show that each cut-sky power spectrum is enhanced, $\Delta C_\ell/C_\ell > 0$, by aberration, with oscillatory features as a function of ℓ . We find that the oscillatory features in $\Delta C_\ell/C_\ell$ is in phase with the slope of the power spectrum $d \ln C_\ell / d \ln \ell$. Furthermore, the enhancement is largest (and exceeds the cosmic variance at each ℓ) when the cut sky is nearest to the north pole (`ring0`) and hence has the maximum asymmetry about the equator. The enhancement is decreasingly prominent when the cut sky moves to lower latitudes, and is least significant for `ring4`. If the cut sky is located in the backward hemisphere, aberration would instead suppress the power spectrum.

This can be understood as follows: Aberration rescales the size of hot/cold spots as described in Eq. (4). In spherical-harmonic space, this results to the angle-dependent rescaling of the multipole moment. For a thin ring centered around latitude $\pi/2 - \theta$, aberration rescales the multipole moment as

$$\ell \rightarrow \ell' = \ell\gamma(1 + \beta \cos \theta), \quad (21)$$

which induces a fractional change,

$$\frac{\Delta C_\ell}{C_\ell} = -\frac{d \ln C_\ell}{d \ln \ell} \beta \cos \theta + \mathcal{O}(\beta^2), \quad (22)$$

in the angular power spectrum. We plot the theoretical prediction as a magenta curve in Fig. 2 which shows an excellent match between Eq. (22) and the simulation (blue dots).

In Fig. 3, we consider two other scenarios: one has half of the forward hemisphere (covering azimuthal angles $0 \leq \phi \leq 180^\circ$) being surveyed ($f_{\text{sky}} = 0.25$), and the other spans the full range of the polar angle with the same azimuthal angle coverage. Again, the maximum of $\simeq 0.8\%$ enhancement in the aberrated power spectrum is seen for the forward case and at large ℓ s the bias dominates over the cosmic variance. For the right-hand-side region, where the survey area encloses both forward and backward regions in a symmetric manner, the aberrated power spectrum shows only very small differences from the unaberrated power spectrum.

What about the theory prediction for these extended regions? For the extended survey region which is defined by the masking function $M(\theta, \phi)$ (which takes 1 for the observed region, and 0 otherwise), we superpose the

³ One can also convolve the two-point correlator in Eq. (16) with the masking window function in harmonic space. However, we find that this procedure takes an impractically long time as it requires two convolutions each of which involves multi-dimensional integration.

⁴ Strictly speaking, this deconvolution only works when the two-point correlator is diagonal in spherical-harmonic space. Although the aberrated temperature map has a non-zero off-diagonal two-point correlation, the effect of these off-diagonal terms must be small given that we were able to reproduce in

Figs. 2–6 the expected residual after deconvolution.

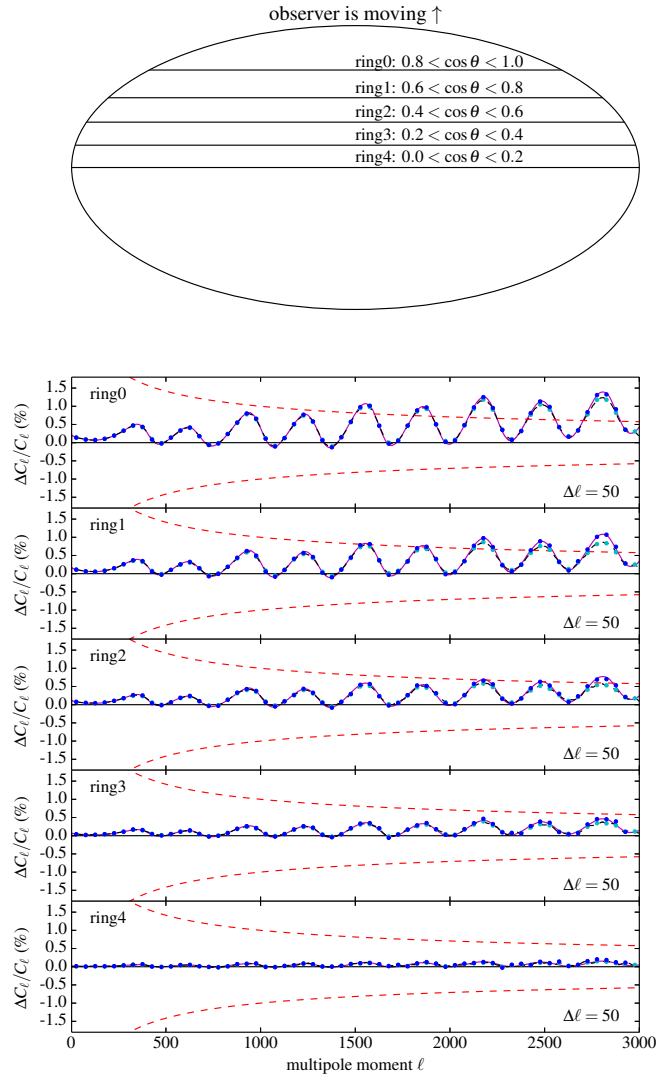


FIG. 2: *Top*: shape of five toy ‘ring’ surveys defined by $0.8 < \cos \theta < 1$ (ring0), $0.6 < \cos \theta < 0.8$ (ring1), $0.4 < \cos \theta < 0.6$ (ring2), $0.2 < \cos \theta < 0.4$ (ring3), and $0 < \cos \theta < 0.2$ (ring4), so that each survey region has $f_{\text{sky}} = 0.1$. The observer is moving upward. The bottom panel shows the fractional differences caused by aberration for each of the five ring survey regions before (cyan points connected by dashed curve) and after (blue points) correcting for the sky mask window function. We also show the cosmic variance with $f_{\text{sky}} = 0.1$ with red dashed curves and the null case ($\Delta C_\ell / C_\ell = 0$) with black solid curves. The magenta solid curves show our analytical approximation of $\Delta C_\ell / C_\ell \approx -(\text{d} \ln C_\ell / \text{d} \ln \ell) \beta \cos \theta$, which reproduces well the simulation. A survey in the backward part of sky would yield residuals with the opposite sign.

residuals Eq. (22) from many thin stripes as

$$\begin{aligned} \frac{\Delta C_\ell}{C_\ell} &\approx -\frac{\beta}{4\pi f_{\text{sky}}} \frac{\text{d} \ln C_\ell}{\text{d} \ln \ell} \int_0^\pi \text{d}(\cos \theta) \cos \theta \int_0^{2\pi} \text{d}\phi M(\theta, \phi) \\ &= -\frac{\text{d} \ln C_\ell}{\text{d} \ln \ell} \beta \langle \cos \theta \rangle \end{aligned} \quad (23)$$

where $\langle \cos \theta \rangle$ is the area-averaged mean of the polar cosine. Note that the residual does not depend on the azimuthal angle because aberration is symmetric in the azimuthal angle. The magenta curve in the left bottom panel of Fig. 3 shows the prediction from Eq. (23)

($\langle \cos \theta \rangle = 0.5$), which provides excellent agreement with the simulation. We also confirm that the linear approximation in Eq. (23) models the residual accurately for the realistic cut skies of Planck, SPT and ACT in Figs. 4–6.

One of the most important implication of Eq. (23) is that the linear order ($\propto \beta$) aberration effect vanishes for surveys with forward/backward symmetry. This is what we see in the right panel of Fig. 3. The tiny, residual $\Delta C_\ell / C_\ell$, with an oscillatory behavior about zero, is negligible compared with cosmic variance. This is expected, because, in linear order, the enhancement of

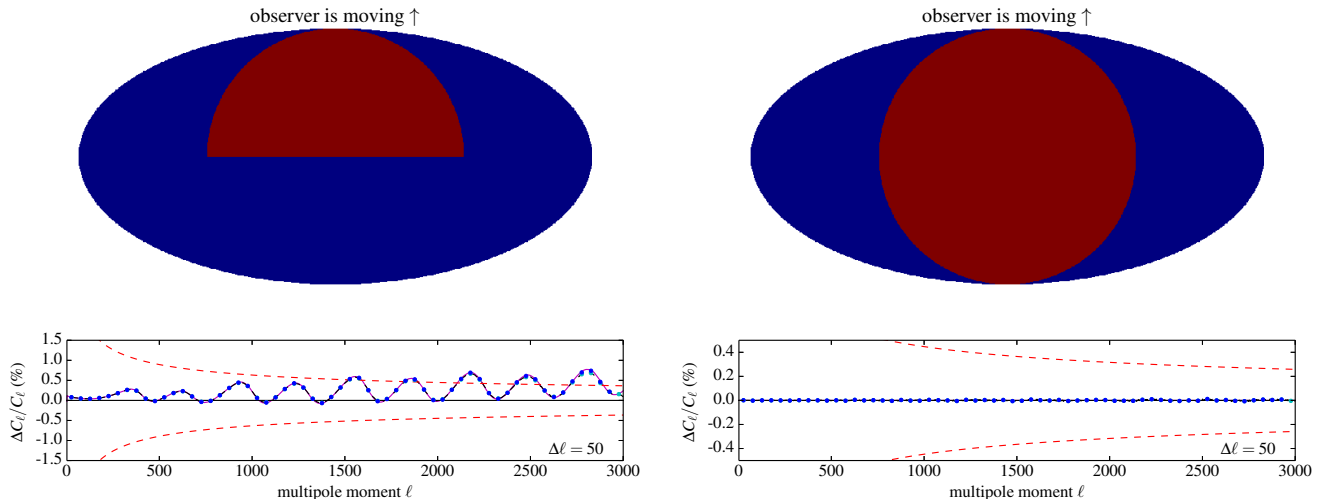


FIG. 3: Shape of two survey regions that cover only half the azimuthal regions. *Left*: surveying only the forward hemisphere, and *right*: surveying the entire range of polar angles. For both regions, the bottom panels show the residual of the observed power spectrum. The curves and symbols are the same as in Fig. 2. Note that $\langle \cos \theta \rangle = 0.5$ and $\langle \cos \theta \rangle = 0$, respectively, for the left and right panels. Thus, the residuals in the symmetric survey region (right panel) suppressed by a factor of β relative to the asymmetric survey in the left panel.

power from the forward direction cancels out the suppression of power from the backward direction. The net effect is thus suppressed by a factor β compared to the asymmetric cases:

$$\frac{\Delta C_\ell}{C_\ell} \approx \frac{\beta^2}{2} \left[\frac{d \ln C_\ell}{d \ln \ell} + \frac{1}{C_\ell} \frac{d^2 C_\ell}{d \ell^2} \ell^2 \langle \cos^2 \theta \rangle \right] \quad (24)$$

Here, $\langle \cos^2 \theta \rangle$ is the area average of the square of the polar cosine. We compare Eq. (24) with the full sky power residual ($\langle \cos^2 \theta \rangle = 1/3$) in the bottom panel of Fig. 1, and find that it captures the overall shape of the full-sky residual very accurately.

B. Planck

As shown in Fig. 4, using the same coordinates as before, Planck masks out the Galactic disk to minimize microwave contamination from our Galaxy, thus leaving a fraction $f_{\text{sky}} \simeq 0.823, 0.697, 0.471$ and 0.40 of the sky for combined mask, lensing mask, HFI mask and HFI Gal040 mask, respectively, for the CMB analysis. The geometry of the sky mask, which can be approximated by a narrow band around zero Galactic latitude, is not symmetric about the boost equator. The degree of forward/backward hemispherical asymmetry depends significantly on the choice of the mask. While the combined mask has roughly same area in the forward hemisphere as in the backward hemisphere ($\langle \cos \theta \rangle = 0.002$), the other masks show larger asymmetries with $\langle \cos \theta \rangle = 0.015,$

$0.07,$ and 0.114 for the lensing mask, HFI mask and HFI Gal040 mask, respectively.

Consequently, it can be seen from the accompanying plot in Fig. 4 that aberration for Planck with a Galactic mask changes dramatically from one mask to another. The combined mask has negligible impact across the whole range of the power spectrum, but the HFI masks show residuals comparable to the cosmic-variance error on small angular scales ($\ell \gtrsim 2000$). Thus, the bias in the deduced power spectrum is at the 1σ level, if the error budget is dominated by cosmic variance. Therefore, the effect of aberration must be corrected differently for the different masks to achieve an unbiased measurement of the temperature power spectrum in the CMB rest frame. As the Galactic masks for different frequency channels show different degrees of backward/forward asymmetry (thus different aberration effects), the aberration, if neglected, may create some tension among power spectra estimated from different frequency channels.

C. SPT, ACT-S, ACT-E

Aberration is also important for ground-based experiments like ACT and SPT, where the sky coverage is smaller and where the mask can be highly asymmetric with respect to the aberration equator.

ACT has so far observed two long narrow strips across the sky. In the left panel of Fig. 5, the southern strip, corresponding to the ACT-S mask, is shown with a sky coverage $f_{\text{sky}} = 0.0075$ [14]. Coincidentally, the southern

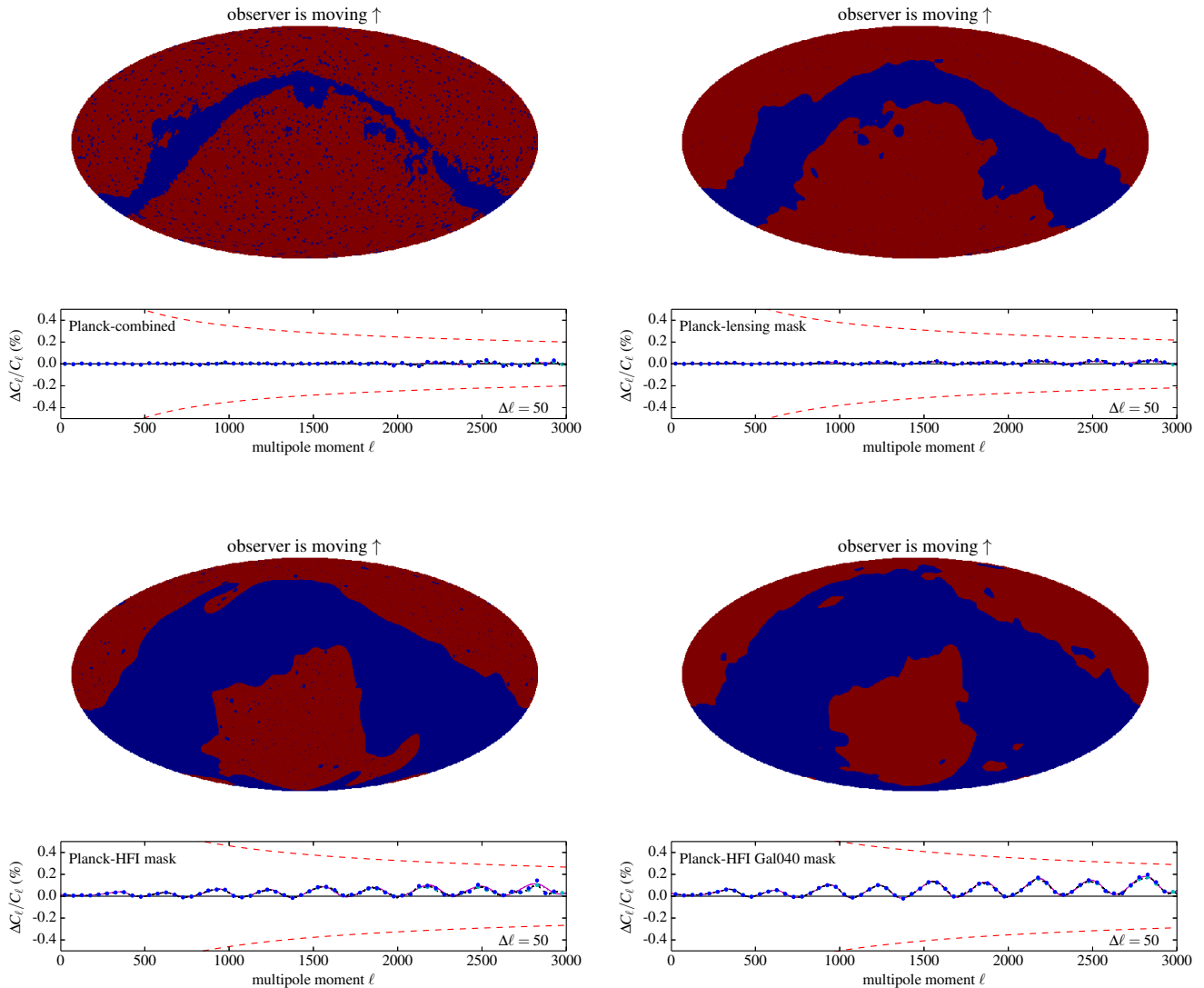


FIG. 4: The shape of the mask (*top panel*) and the residual of power spectrum (*bottom panel*) for four different masks from Planck satellite: Combined mask (*top left*), Lensing mask (*top right*), HFI mask (*bottom left*) and HFI Gal040 mask (*bottom right*). The mask is drawn in coordinates where the observer is moving upward. The bottom panel of each figure shows the residual effect of aberration before (cyan points connected by dashed curve) and after (blue points) the sky-mask deconvolution along with the cosmic-variance error (red dashed curve) with $f_{\text{sky}} = 0.823, 0.697, 0.471$ and 0.400 for Combined, lensing, HFI, HFI Gal040 mask, respectively. Each point shows the binned average with the indicated width, and the magenta curve shows the prediction from the linear theory in Eq. (23) with $\langle \cos \theta \rangle = 0.002$ (combined mask), 0.015 (lensing mask), 0.07 (HFI mask) and 0.114 (HFI Gal040 mask). Note that aberration residual is different for different masks. If cosmic variance dominates the error budget down to $\ell = 3000$, aberration biases the amplitude of the angular power spectrum to $0.3\sigma, 0.4\sigma, 1\sigma,$ and 1.6σ for combined, lensing, HFI and HFI Gal040 mask, respectively.

strip is roughly symmetric about the aberration equator, with the part in the backward hemisphere slightly larger than that in the forward hemisphere. Therefore, the cut-sky power spectrum for the ACT-S mask is only marginally suppressed by aberration, with $|\Delta C_\ell/C_\ell| < 0.25\%$. The equatorial strip, or ACT-E mask, has a sky coverage of $f_{\text{sky}} = 0.0073$, and lies completely in the backward hemisphere [14], as shown in the right panel of

Fig. 5. As a result, our simulations exhibit a more significant power suppression from aberration, as large as $\approx 1\%$ in magnitude.

Also, as shown in Fig. 6, SPT has surveyed a region in the sky with $f_{\text{sky}} = 0.06$. It can be seen that a much larger fraction of the survey region lies in the backward hemisphere, which leads to as much as an 0.4% suppression of the power spectrum for $\ell \gtrsim 1000$ caused by the

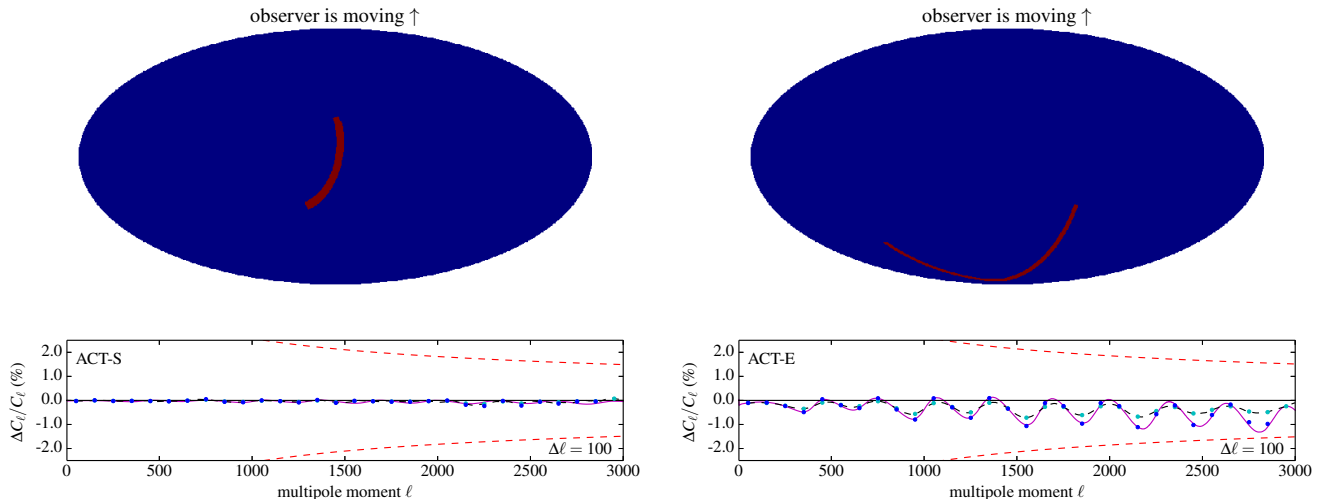


FIG. 5: The same as Fig. 4, but for two of the ACT regions: ACT-S(*left*) and ACT-E(*right*). The cosmic-variance error (red dashed curve) is calculated with $\Delta\ell = 100$ and $f_{\text{sky}} = 0.0075, 0.0073$ for ACT-S and ACT-E, respectively. The magenta curve shows the prediction from the linear theory in Eq. (23) with $\langle\cos\theta\rangle = -0.18$ (ACT-S) and -0.85 (ACT-E). If cosmic variance dominates the error budget down to $\ell = 3000$, aberration biases the amplitude of the angular power spectrum to 0.2σ and 1σ for ACT-S and ACT-E, respectively.

observer’s peculiar velocity.

Therefore, our simulations unambiguously demonstrate that both the ACT and SPT experiments suffer from systematic power suppression on small scales from aberration. As the Figures indicate, the suppression is small, in each ℓ band plotted, compared with the statistical error. Still, the systematic bias induced by aberration in the *complete* data set, and thus on the inferred cosmological parameters, is in fact significant. For example, the SPT power spectrum measured to $\ell_{\text{max}} \simeq 3000$ from 6% of the sky is obtained from $\simeq 5.6 \times 10^5$ modes, implying a cosmic-variance error of $\simeq 0.0013$ on the overall amplitude. Thus, the systematic suppression in SPT due to aberration may be as large as a few- σ effect and cannot be ignored. Given the smaller suppression and smaller sky coverage in ACT-S, the effects of aberration are smaller compared with the statistical error. However, for ACT-E, the systematic suppression due to aberration may be a roughly $\simeq 1\sigma$ effect. We surmise that aberration may be at least partially responsible for the small tension between cosmological parameters inferred from ACT, SPT, and Planck[23].

D. Aberration effect on cosmological parameters

In the previous Sections, we have shown that the effect of aberration on the measurement of the temperature power spectrum on part of the sky can be accurately modeled by the simple re-scaling of multipole moments in Eq. (21). Therefore, ignoring this re-scaling due to

aberration biases all of the ‘horizontal’ information encoded in the temperature power spectrum. For example, ignoring aberration would shift the sound-horizon angle θ_* by $\Delta\theta_*/\theta_* = -\Delta\ell/\ell \simeq -\beta\langle\cos\theta\rangle$ which is -0.014% with the Planck Gal040 mask, and goes up to 0.03% and 0.1% with, respectively, the SPT and ACT-E survey footprints. The level of bias in measuring θ_* is comparable to the reported 1- σ (68% confidence level) range of measuring θ_* ($\sim 0.06\%$) from the Planck collaboration [11]⁵.

How does this shift affect the cosmological parameters? A full answer to this question requires an in-depth analysis of the likelihood function in the parameter space. We simplify the situation by fixing parameters which determine the shape of the power spectrum, $\{\Omega_m h^2, \Omega_b h^2, \tau, n_s, A_s\}$ so that the shift in the sound-horizon angle θ_* mainly causes bias in the angular-diameter distance $D_A(z_*)$ to the last-scattering surface. Assuming a flat universe, this leaves us with two parameters: the Hubble parameter $H_0 = 100h$ Mpc/km/s and dark-energy equation of state w_{de} ⁶. With the best-fitting Λ CDM parameters (“Planck+lensing+WP+highL” column in the Table 5 of [11]), we find that aberration induces an 0.072% bias on H_0 (that moves maximum likelihood value from $h = 0.6794$ to $h = 0.6799$) and -0.16% bias on w for Planck HFI (Gal040) mask, and it goes up to -0.15%

⁵ Planck collaboration has also noted this shift of θ_* in footnote 13 (page 9) of [11] and page 2 of [4].

⁶ Fixing $\Omega_m h^2$ in flat universe also fixes dark energy density parameter Ω_{de} for a given h .

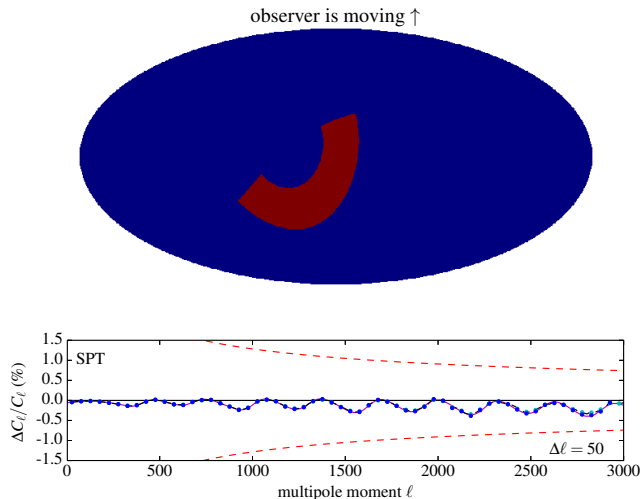


FIG. 6: The same as Fig. 4 and Fig. 5, but for SPT footprint. The cosmic-variance error (red dashed curve) is calculated with $\Delta\ell = 50$ and $f_{\text{sky}} = 0.06$, and the magenta curve shows the prediction from the linear theory in Eq. (23) with $\langle \cos\theta \rangle = -0.26$. If cosmic variance dominates the error budget down to $\ell = 3000$, aberration biases the amplitude of the angular power spectrum sky-mask deconvolution along with the cosmic-variance error to 1.3σ .

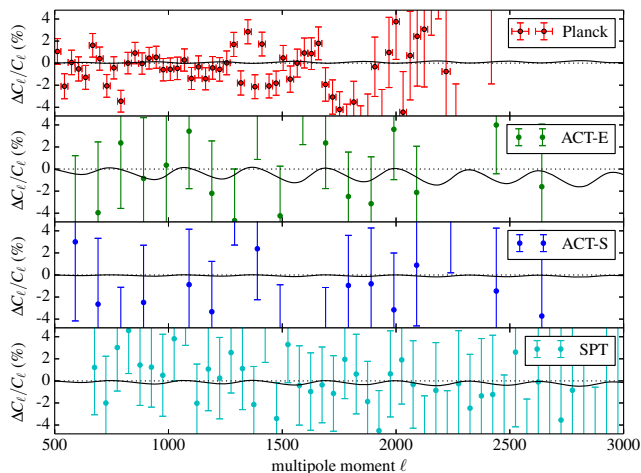


FIG. 7: The power-spectrum residuals for Planck, ACT-E, ACT-S, and SPT (from *top to bottom*) with respect to the best-fitting power spectrum from combining Planck, lensing, WMAP polarization and high ℓ (ACT and SPT). The data points are the measured binned power spectrum, and the error bars include both cosmic variance and instrumental noise. The expected aberration residual with $\beta = 0.00123$ is shown as the black solid curve. With the error bars used in this plot, aberration biases the amplitude of the angular power spectrum by 0.47σ , 0.07σ , 0.64σ , and 0.34σ for Planck (Gal040 mask), ACTS, ACTE and SPT, respectively.

(H_0), 0.34% (w) for SPT, and -0.51% (H_0), 1.14% (w) for ACT-E. Therefore, it is important to correct for aberration in order to achieve a percent level accuracy on parameters such as H_0 and w . Moreover, when combining parameters from different surveys, ignoring aberration would enhance the tension as cosmological parameters from Planck and ACT/SPT are biased toward opposite directions.

Finally, to quantify more precisely the magnitude of the effect in current data set, Fig. 7 shows power-spectrum residuals with respect to the best-fitting Λ CDM model (“Planck+lensing+WP+highL” column in the Table 5 of [11]) for the four CMB surveys we consider here: Planck [22], ACT-E, ACT-S, and SPT [24]. The error bars here include not only cosmic variance, but also the instrumental noise. With the effects of instrumental noise for the existing data included, the magnitude of the effect of aberration relative to the statistical error is reduced. The systematic bias induced by aberration in the amplitude of the power spectrum becomes 0.47σ , 0.64σ and 0.34σ for Planck HFI (Gal040 mask), ACT-E and SPT, respectively. This is smaller than what would be inferred considering only cosmic variance, but still not negligible.

We furthermore note that the effects of aberration may have a more profound impact on power-spectrum and cosmological-parameter measurements from future experiments that survey larger regions of the sky (especially those that are skewed toward one of the boost poles). It will also become more significant for forthcoming experiments that include polarization, an issue we address in a forthcoming publication [25]. Also, aberration might affect higher order statistics of the CMB both on the full-sky and for the cut-sky in subtle ways that should be considered more carefully.

V. CONCLUSION

While aberration affects full-sky measurements of the power spectrum only at order β^2 [Eq. (24)], the effect on the power spectrum inferred from maps with partial-sky coverage arise at linear order in β [Eq. (23)] and may thus be much larger. The effects of aberration are magnified further as a consequence of the steep falloff of the power spectrum ($C_\ell \propto \ell^{-7}$) at the high ℓ probed by several current and forthcoming CMB experiments. In total, the effect can constitute a systematic bias as large as $\simeq 1\%$, considerably larger than statistical errors in current measurements, in measurements of the power spectrum. It must therefore be explored in detail.

We have developed a novel formalism to account for the effects of aberration on measurements of the CMB temperature power spectrum from maps with partial sky coverage. Our analysis improves upon prior work by going to higher orders in β , thus extending the validity of analytic calculations to multipole moments $\ell \gtrsim \beta^{-1} \simeq 800$. Our harmonic-space approach to de-boosting also provides a

more effective and computationally efficient way to deal with the effects of window functions and pixelization than the real-space approach explored in prior work.

We then used these new algorithms to explore in detail the effects of aberration on Planck, ACT, and SPT. We conclude that the effect of aberration for Planck depends strongly on the choice of the mask, and the mask used for power spectrum analysis of data with HFI (Gal040) shows $\simeq \sigma$ level changes due to aberration. More importantly, as the effect of aberration varies from one mask to another, unbiased estimation of temperature power spectrum would require cleaning the aberration effect before combining the power spectra from different frequency channels. We also conclude that the systematic bias in current SPT data affects measurements of the power spectrum at the $\simeq \sigma$ level and thus cannot be ignored. The effects in current ACT-S data are negligible, but those in ACT-E arise at the $\simeq \sigma$ level. We surmise that aberration may be responsible for part of the small tension between power spectra inferred from SPT, ACT, and Planck, and thus also for the values of cosmological parameters inferred from these experiments.

We also note that the magnitude of the effects of aberration, relative to the statistical error, may become larger for future measurements that survey larger regions of the sky, especially for those that are aligned or anti-aligned with our peculiar velocity with respect to the CMB rest frame. Aberration will also become more important with forthcoming experiments in which the statistical power is extended with measurements of the polarization. A forthcoming paper [25] will deal with aberration effects on the polarization.

Finally, while the focus in our discussion has been on measurements of the *primordial* power spectrum, and the values of cosmological parameters inferred, aberration affects the measurement of *all* fluctuations. This includes CMB fluctuations from secondary extragalactic sources, and it will also include measurements of other cosmic backgrounds such as fluctuations of the 21-cm background. High-resolution measurement of weak lensing may also be affected by aberration. As the analytical calculations in Eqs. (23)–(24) come solely from relativistic beaming and does not depend on the specific shape of the energy spectrum, it should also be useful for analyzing the power spectra for these other maps.

Our harmonic-space approach to deboosting will also be useful for measurements of higher-order statistics as well. Without them, estimators for the bispectrum and trispectrum may be affected by aberration.

Acknowledgments

The authors acknowledge Anthony Challinor, Duncan Hanson, Gilbert Holder, Arthur Kosowsky, Eiichiro Komatsu, David Larson, Antony Lewis and Aditya Rotti for useful discussions, and Antony Lewis for pointing out the Planck mask used for the power spectrum analysis of

HFI data. Some of the results in this paper have been derived using the HEALPIX [20] package. This work was supported by DoE SC-0008108, NASA NNX12AE86G, and NSF 0244990. MK acknowledges the hospitality of the Aspen Center for Physics, supported in part by the National Science Foundation under Grant No. PHYS-1066293. LD is supported by the William Gardner Fellowship.

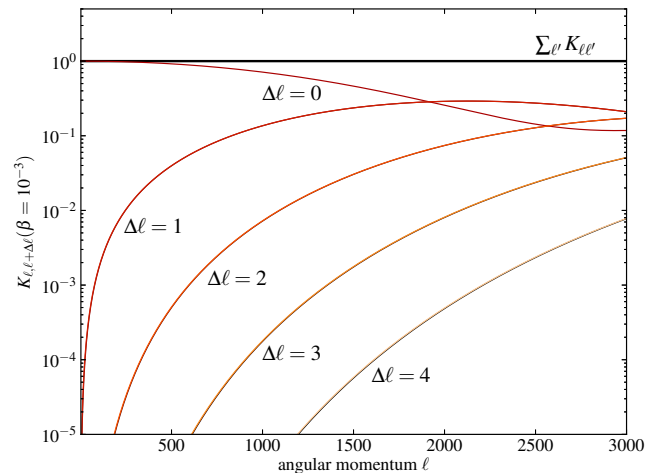


FIG. 8: The power transfer matrix, $K_{\ell\ell'}(\beta)$ [Eq. (A2)], for $\beta = 10^{-3}$. The results for $\ell > \ell'$ and $\ell < \ell'$ are the same to within the thickness of the curve. For smaller angular scales ($\ell > 200$), more than 1% of the temperature fluctuation is transferred to adjacent multipoles, and power leakage reaches about 30% for $\ell \simeq 1000$. At $\ell = 3000$, only about 12% of the power is left at the same multipole ($\Delta\ell = 0$). The *total* curve at the top shows $\sum_{\ell'} K_{\ell\ell'}$.

Appendix A: Unitarity of the aberration kernel and approximate power conservation

Ref. [5] derived a relation, $C_\ell^{\text{obs}} = C_\ell(1 + 4\beta^2 + \dots)$, implying that the full-sky power spectrum for the boosted map differs by no more than $\simeq 4\beta^2 \simeq 6 \times 10^{-6}$ from that for the original map. This analytic result does not necessarily hold, however, at $\ell \gtrsim 800$, as discussed above. Numerical evaluation of power spectra on boosted maps have since then confirmed [17], though, that the full-sky power spectrum is very nearly unchanged. Here we show that this result follows directly from unitarity of the aberration kernel.

From Eq. (16), we calculate the observed angular

power spectrum,

$$\begin{aligned} C_\ell^{(\text{obs})} &= \frac{1}{2\ell+1} \sum_m \left\langle \left| a_{\ell m}^{(\text{obs})} \right|^2 \right\rangle \\ &= \frac{1}{2\ell+1} \sum_{\ell' m} \left[\mathcal{K}_{\ell' m}^{\ell' m}(\beta) \right]^2 C_{\ell'} = \sum_{\ell'} K_{\ell \ell'}(\beta) C_{\ell'}, \end{aligned} \quad (\text{A1})$$

where we defined the power transfer matrix

$$K_{\ell \ell'}(\beta) \equiv \frac{1}{2\ell+1} \sum_m \left| \mathcal{K}_{\ell' m}^{\ell' m}(\beta) \right|^2. \quad (\text{A2})$$

Unitarity of the aberration kernel arises because an aberration followed by an inverse aberration (an aberration with negative velocity $-\beta$) should lead to the original map. From Eq. (12), we find [18], [e.g., 5, 18]

$$\mathcal{K}_{\ell' m}^{\ell' m}(\beta) = \mathcal{K}_{\ell' m}^{\ell' m}(-\beta). \quad (\text{A3})$$

Then, the aberration followed by inverse-aberration is

$$\begin{aligned} a_{\ell' m}'' &= \sum_{\ell'} \mathcal{K}_{\ell' m}^{\ell' m}(-\beta) \left[\sum_{\ell} \mathcal{K}_{\ell' m}^{\ell' m}(\beta) a_{\ell m} \right] \\ &= \sum_{\ell} \sum_{\ell'} \mathcal{K}_{\ell' m}^{\ell' m}(\beta) \mathcal{K}_{\ell' m}^{\ell' m}(\beta) a_{\ell m} = a_{\ell m}, \end{aligned} \quad (\text{A4})$$

which completes the proof of the unitarity,

$$\sum_{\ell'} \mathcal{K}_{\ell' m}^{\ell' m}(\beta) \mathcal{K}_{\ell' m}^{\ell' m}(\beta) = \delta_{\ell' \ell}. \quad (\text{A5})$$

This result implies that the power transfer matrix satisfies $\sum_{\ell'} K_{\ell \ell'} = 1$. Since, roughly speaking, aberration shifts multipole moments $\ell \rightarrow \ell(1 \pm \beta)$ in the forward/backward directions, the effect of aberration on a full-sky map is to smear the power over a range $\Delta\ell \simeq \beta\ell$. Numerical evaluation of the kernel, shown in Fig. 8, verifies that the support of the power transfer matrix $K_{\ell, \ell+\Delta\ell}$ is limited to $\Delta\ell \lesssim \beta\ell$.

Smearing of the power spectrum C_ℓ over a range $\beta\ell$ then leads to a power change $\simeq (\partial^2 C_\ell / \partial \ell^2) \beta^2 \ell^2$. Thus, the smallness of the shift in the full-sky power spectrum at $1000 \lesssim \ell \lesssim 3000$ is seen to be a consequence of the fact that $\beta\ell \simeq 1$ is small compared with the spacing $\Delta\ell \simeq 200$ between the acoustic peaks.

-
- [1] D. J. Fixsen, E. S. Cheng, J. M. Gales, J. C. Mather, R. A. Shafer and E. L. Wright, *Astrophys. J.* **473**, 576 (1996) [arXiv:astro-ph/9605054]; D. J. Fixsen, *Astrophys. J.* **707**, 916 (2009) [arXiv:0911.1955 [astro-ph.CO]].
- [2] P. M. Lubin, G. L. Epstein, and G. F. Smoot, *Phys. Rev. Lett.* **50**, 616 (1983); D. J. Fixsen, E. S. Cheng, and D. T. Wilkinson, *Phys. Rev. Lett.* **50**, 620 (1983); A. Kogut *et al.*, *Astrophys. J.* **419** 1 (1994); A. Kogut *et al.*, *Astrophys. J.* **419**, 1 (1993) [arXiv:astro-ph/9312056].
- [3] G. Hinshaw *et al.* [WMAP Collaboration], *Astrophys. J. Suppl.* **180**, 225 (2009) [arXiv:0803.0732 [astro-ph]].
- [4] N. Aghanim *et al.* [Planck Collaboration], arXiv:1303.5087 [astro-ph.CO].
- [5] A. Challinor and F. van Leeuwen, *Phys. Rev. D* **65**, 103001 (2002) [arXiv:astro-ph/0112457].
- [6] A. Kosowsky and T. Kahniashvili, *Phys. Rev. Lett.* **106**, 191301 (2011) [arXiv:1007.4539 [astro-ph.CO]].
- [7] L. Amendola, R. Catenà, I. Masina, A. Notari, M. Quartin and C. Quercellini, *JCAP* **1107**, 027 (2011) [arXiv:1008.1183 [astro-ph.CO]].
- [8] S. Burles and S. Rappaport, *Astrophys. J. Lett.* bf 641, L1 (2006) [arXiv:astro-ph/0601559].
- [9] T. S. Pereira, A. Yoho, M. Stuke and G. D. Starkman, arXiv:1009.4937 [astro-ph.CO].
- [10] G. Jungman, M. Kamionkowski, A. Kosowsky and D. N. Spergel, *Phys. Rev. Lett.* **76**, 1007 (1996) [arXiv:astro-ph/9507080]; G. Jungman, M. Kamionkowski, A. Kosowsky and D. N. Spergel, *Phys. Rev. D* **54**, 1332 (1996) [astro-ph/9512139].
- [11] P. A. R. Ade *et al.* [Planck Collaboration], arXiv:1303.5076 [astro-ph.CO].
- [12] K. T. Story, C. L. Reichardt, Z. Hou, R. Keisler, K. A. Aird, B. A. Benson, L. E. Bleem and J. E. Carlstrom *et al.*, arXiv:1210.7231 [astro-ph.CO].
- [13] Z. Hou, C. L. Reichardt, K. T. Story, B. Follin, R. Keisler, K. A. Aird, B. A. Benson and L. E. Bleem *et al.*, arXiv:1212.6267 [astro-ph.CO].
- [14] S. Das, T. Louis, M. R. Nolta, G. E. Addison, E. S. Battistelli, J. R. Bond, E. Calabrese and D. C. M. J. Devlin *et al.*, arXiv:1301.1037 [astro-ph.CO].
- [15] J. L. Sievers, R. A. Hlozek, M. R. Nolta, V. Acquaviva, G. E. Addison, P. A. R. Ade, P. Aguirre and M. Amiri *et al.*, arXiv:1301.0824 [astro-ph.CO].
- [16] A. Notari and M. Quartin, *JCAP* **1202**, 026 (2012) [arXiv:1112.1400 [astro-ph.CO]].
- [17] A. Yoho, C. J. Copi, G. D. Starkman and T. S. Pereira, *Mon. Not. R. Astron. Soc.* **432**, 2208 (2013) [arXiv:1211.6756 [astro-ph.CO]].
- [18] J. Chluba, *Mon. Not. R. Astron. Soc.* **415**, 3227 (2011) [arXiv:1102.3415 [astro-ph.CO]].
- [19] E. Komatsu *et al.* [WMAP Collaboration], *Astrophys. J. Suppl.* **192**, 18 (2011) [arXiv:1001.4538 [astro-ph.CO]].
- [20] K. M. Gorski, E. Hivon, A. J. Banday, B. D. Wandelt, F. K. Hansen, M. Reinecke and M. Bartelman, *Astrophys. J.* **622**, 759 (2005) [astro-ph/0409513].
- [21] E. Hivon, K. M. Gorski, C. B. Netterfield, B. P. Crill, S. Prunet and F. Hansen, *Astrophys. J.* **567**, 2 (2002)

- [astro-ph/0105302].
- [22] P. A. R. Ade *et al.* [Planck Collaboration], arXiv:1303.5075 [astro-ph.CO].
- [23] E. Di Valentino, S. Galli, M. Lattanzi, A. Melchiorri, P. Natoli, L. Pagano and N. Said, Phys. Rev. D **88**, 023501 (2013) [arXiv:1301.7343 [astro-ph.CO], arXiv:1301.7343 [astro-ph.CO]].
- [24] E. Calabrese, R. e A. Hlozek, N. Battaglia, E. S. Battistelli, J. R. Bond, J. Chluba, D. Crichton and S. Das *et al.*, arXiv:1302.1841 [astro-ph.CO].
- [25] L. Dai *et al.*, in preparation.